Radiative transfer modelling of dust devils

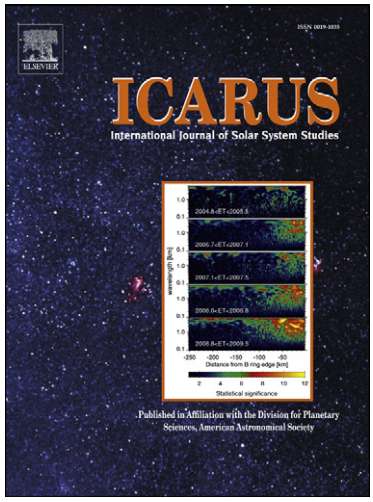

Radiative Transfer Modelling of Dust Devils

Jonathon P. Mason, Manish R. Patel, Stephen R. Lewis

PII: S0019-1035(12)00472-1
DOI: http://dx.doi.org/10.1016/j.icarus.2012.11.018
Reference: YICAR 10459

To appear in: *Icarus*

Please cite this article as: Mason, J.P., Patel, M.R., Lewis, S.R., Radiative Transfer Modelling of Dust Devils, *Icarus* (2012), doi: http://dx.doi.org/10.1016/j.icarus.2012.11.018

Radiative Transfer Modelling of Dust Devils

Jonathon P. Mason, [a] Manish R. Patel, [a] and Stephen R. Lewis, [a]

[a] The Open University, Walton Hall, Milton Keynes, MK7 6AA

Pages: 34

Tables: 1

Figures: 12

Proposed Running Head:

Radiative Transfer Modelling of Dust Devils

Editorial correspondence to:

Mr Jonathon P Mason

The Open University

Walton Hall

Milton Keynes

MK7 6AA

Phone: +44 1908 655543

E-mail address: j.p.mason@open.ac.uk

Abstract:

Dust devils are particle laden convective vortices that form at the base of convective plumes. They are typically observed in dry desert climates on Earth and have been observed to form frequently on Mars. Meteorological measurements have also indicated that martian surface spacecraft have experienced numerous dust devil transits. To date, the characterisation of dust devils through the interpretation of spectral measurements of sunlight taken during a transit has yet to be investigated. Such measurements would provide valuable information of the physical size, dust load and internal structure of dust devils. A Monte Carlo Radiative Transfer (MCRT) model was developed to simulate the attenuation of sunlight through a dust devil and to investigate the observed spectral variation during such an event. The predicted spectral signature resulting from a dust devil transit is highly dependent on the method of observation. The scattered light flux increases during the transit with the magnitude dependent on the dust concentration, making it sensitive to the internal dust distribution. This dependence is not observed for the total light flux which experiences a decrease and is strongly dependent on the total extinction through the vortex and insensitive to how the dust is distributed. The implication of this work is that separate *in situ* measurement of both the total *and* scattered flux is crucial for characterising dust devils and such measurements provide a powerful tool that could be exploited by future Mars missions.

Key Words: Dust devil, Monte Carlo, Dust, Light scattering, Mars, Earth atmosphere

1 Introduction

Aeolian mineral dust can have a large impact on the radiation budget of planetary atmospheres such as those surrounding the Earth and Mars. This dust can absorb solar and infrared radiation resulting in localised warming of the atmosphere (positive radiative forcing) and scatter incoming electromagnetic radiation back to space, resulting in cooling of the atmosphere (negative radiative forcing). The balance between absorption and scattering determines whether the aeolian dust acts to cool or warm the surrounding atmosphere (Alpert *et al.*, 1998) and highlights the importance of accurate retrieval of the dust particle single scattering properties, specifically the single scattering albedo (ω_0), defined as the ratio of the scattered solar radiation to the total solar radiation removed by both scattering and absorption. One method used to retrieve the single scattering properties is to fit the observed attenuated spectrum to radiative transfer model outputs. However, accurate modelling of the light transmission through a dusty environment can be extremely difficult, especially at high dust concentrations, where the single scattering approximation is inadequate to accurately describe the diffuse component. The Monte Carlo Radiative Transfer (MCRT) method has been used successfully in many different fields to accurately describe multiple scattering scenarios in significantly different environments. Witt (1977) applied MCRT to interstellar grains by looking at reflectance nebulae and has shown that MCRT can be applied to the multiple scattering problem. MCRT was employed by Vincendon and Langevin (2010) to simulate the impact of aerosols on the remote sensing of the surface of Mars and Titan. More relevant to this study, Metzger *et al*. (1999b) used a MCRT to simulate the scattered diffuse component of martian dust devils observed by the Imager for Mars Pathfinder (IMP).

The purpose of this paper is to describe a MCRT model that is used to simulate the transmission of sunlight through dust devil vortices. The simulated spectral variation during a dust devil transit over a spectrometer is investigated to determine whether the dust load, size and internal structure of the vortex can be estimated from a dust devil transit signature (defined as the measured light curve as a function of distance). The transmission of sunlight through the vortex depends on how the dust is

distributed internally and the internal structure of the vortex (in terms of the core diameter). Therefore the internal structure and dust distribution of dust devils is explored explicitly, comparing the assumption of a uniform dust concentration to one with a relatively dust free central vortex surrounded by walls of a higher dust concentration. Finally, the effect on the transit signature due to variations in the entrained dust particle single scattering properties is investigated to determine the possibility of retrieval of the dust particle optical properties. Dust devils have yet to be characterised by interpreting *in situ* spectral measurements and this will be an invaluable technique for martian surface landers, which experience hundreds of dust devil transits during their life but may be unable to provide images of all encounters to determine their physical parameters.

This paper discusses previous retrievals of aeolian dust optical properties on Earth and investigations into the characteristics of terrestrial and martian dust devils. The developed MCRT model is described, followed by an analysis into the photon propagation through the model volume for different dust concentrations and optical scattering properties. Finally, the predicted transit signatures of dust devils with different internal structures and dust distributions are provided and the effects of changes to the dust single scattering properties discussed.

1.1 Airborne desert dust on Earth

The optical properties of airborne terrestrial dust remains a debated issue (Dubovik *et al.*, 2000; Kaufman *et al.*, 2001a). Expressed in terms of its imaginary refractive index, n_i, (a measure of the amount electromagnetic radiation absorbed by the material) the recognised value by the World Meteorological Organisation (WMO) is 0.008 at 500 nm (WMO,1983) and corresponds to a single scattering albedo (ω_0) of 0.63. Another study by Levin *et al*. (1980) predicted a smaller n_i of 0.003 ($\omega_0 \sim 0.87$). For desert dust, ω_0 has been simulated to have values between 0.63 and 0.87 at 500 nm (Shettle and Fenn, 1976; WMO, 1983; Hess *et al.*, 1998). To exacerbate the issue, Fouquart *et al*. (1987), using aircraft radiation measurements, determined an ω_0 value for the broadband solar spectrum to be 0.95 for Saharan dust, indicating significantly less absorption. Furthermore, recent

retrievals of ω_0 for desert dust (Dubovik *et al.*, 2000; Kaufman *et al.*, 2001b) agree with the results of Fouquart, *et al*. (1987) with $\omega_0 > 0.9$ for the majority of the solar spectrum, indicating that the dust acts to cool the atmosphere. It should be recognised that the uncertainty in the retrieved single scattering properties is likely due to natural variability resulting from heterogeneity in the dust material at different global locations. This also applies at local spatial scales where the composition of the source material can vary significantly. The large uncertainty in the single scattering properties of suspended desert dust can lead to contrasting predictions of their radiative forcing, with a small change in ω_0 from 0.95 to 0.85 leading to positive radiative forcing instead of negative forcing (Hansen *et al.*, 1997). This highlights the importance of accurate determination of ω_0 at visible wavelengths. Dust devils are efficient at lofting small particles into the atmosphere (Greeley *et al.*, 2006) and therefore knowledge of the dust optical properties and the amount of material lofted into the atmosphere enables the radiative effect of dust devils on the local atmosphere to be determined.

1.2 Dust devils

Dust devils are low pressure, warm core vortices which usually occur during the summer season in arid locations around the world (Ives, 1947). A dust devil is a special type of vertical convective current characterised by dust entrained around the upward convective flow. Many in-depth field studies of terrestrial dust devils have been carried out to date (Sinclair, 1966; Ryan and Carroll, 1970; Sinclair, 1974; Metzger, 1999a; Greeley *et al.*, 2003; Balme and Greeley, 2006).

Laboratory experiments have also been conducted to investigate different components of dust devil vortices. Greeley *et al*. (2003) constructed a vortex generator (The Arizona State University Vortex Generator, ASUVG) to simulate terrestrial and martian dust devils. Their experiments showed that the pressure drop (ΔP) at the vortex core provides an additional lift component, making dust devils more efficient at removing dust from surfaces than boundary layer winds. Using the ASUVG, Neakrase *et al*. (2006) and Neakrase and Greeley (2010a) conducted dust and sediment flux experiments at Earth and Mars atmospheric pressures and found that the sediment flux is related to the

vortex intensity, which itself is dependent on the ΔP at the core. Their experiments showed that vortices of different sizes could yield the same ΔP at the core and concluded that the vortex size is less important for sediment lifting than the ΔP at the core. The vertical flux of dust (particles < 2 μm in diameter) was found to increase exponentially with increasing tangential velocity but decrease exponentially with increasing core radii demonstrating that smaller vortices experience higher vertical dust fluxes. A similar relationship to the core pressure drop was also reported with an exponential increase in vertical dust flux for larger ΔP. Furthermore, the effects of surface roughness on dust devil dynamics was explored by Neakrase and Greeley (2010b) for terrestrial and martian dust devils. They found a correlated increase in the vortex size with increasing surface roughness, while the tangential velocity was observed to decrease. The expansion of the vortex reduces the energy available and will eventually impede additional lifting of surface material. However, Neakrase and Greeley (2010b) showed that small increases in surface roughness can reduce the threshold required to lift fine particles (< 100 μm), enhancing the sediment flux of weaker dust devils beyond that which would be expected. For larger increases in surface roughness the ΔP and tangential velocities are reduced, decreasing the vertical flux of surface material. While the theoretical modelling presented in this paper focuses on the applications to field studies, measuring the light flux through laboratory generated dust devils would allow investigations into the effect of dust particle size on the spectral attenuation and how the size of the particles being suspended influences the spatial distribution of dust in the dust devil interior. Since the dust particle size and the physical dimensions of laboratory generated dust devils can be constrained, these measurements would be more directly comparable to model predictions than those taken in the field.

Dust devils are not a unique phenomenon to the Earth, with observations from Viking 1 and 2, Mars Pathfinder (MPF), Mars Global Surveyor, Odyssey and Mars Exploration Rovers (MER), among others, showing that they form frequently on the martian surface (Ryan and Lucich, 1983; Thomas and Gierasch, 1985; Metzger *et al.*, 1999b; Ferri *et al.*, 2003; Fisher *et al.*, 2005; Cantor *et al.*, 2006; Greeley *et al.*, 2010). While dust devils on the two planets are similar, they play very

different roles on their respective planets. On Earth they are secondary to boundary layer winds in the dust cycle and only play a minor role except possibly in arid regions. In contrast, on Mars they maintain the constant aeolian dust background, especially in northern summer, and play a major role in the rapid transport of fine particulates into the martian planetary boundary layer, affecting the atmospheric heating rate. Dust devils also influence the surface albedo through the formation of tracks as they transverse the surface (Balme *et al.*, 2003; Whelley and Greeley, 2006). From column opacity measurements taken by IMP, Metzger *et al.* (1999b) estimated the particle loading for a dust devil to be 70 mg m^{-3} and, assuming a vertical wind velocity of 7 ms^{-1}, they determined the vertical flux of material into the atmosphere to be 0.49 g m^{2} s^{-1}. Using the thermodynamic theory for dust devils of Rennó *et al*. (1998) and MPF meteorological data, Ferri *et al*. (2003) estimated the vertical velocity of martian dust devils to be 20 ms^{-1} and determined the rate at which dust is injected into the atmosphere by dust devils to be two orders of magnitude higher than the dust settling rate. The Mars Exploration Rover (MER) Spirit observed three full seasons of dust devil activity within Gusev crater during mars years (MY) 27, 28 and 29 (Greeley *et al.*, 2010). Over all seasons the vertical wind speeds of the dust devils were observed to be between 0.04–17.0 ms^{-1} with the vertical dust flux ranging between 0.004–0.46 g m^{2} s^{-1}. Martian dust devils are not confined to lower latitudes, meteorological data measured at the Phoenix landing site (68° N) showed that during its operational life time the lander experienced 502 identifiable encounters with a convective vortex or dust devil (Ellehoj *et al.*, 2010).

2 Radiative transfer in dusty environments

2.1 Model description

The scattering of sunlight by dust grains entrained in a dust devil vortex was modelled using the Monte Carlo method (Cashwell and Everett, 1959; Witt, 1977; Whitney, 2011). The model geometry and coordinate system are illustrated in Fig. 1. The Cartesian coordinate system (*X*, *Y*, *Z*) has its origin at the vortex centre and the vertical *Z*-axis is directed along the axis of symmetry of the vortex flow,

normal to the *X*-*Y* plane. The position of the individual photons is given by their (*X, Y, Z*) coordinates while their direction vector, $P_{v,}$ is described by the directional cosines (u_x, u_y, u_z), which are calculated from the angles θ and φ. Assuming that the Sun is a point source, the incident photons are plane-parallel, travelling in the $+X$ and $-Z$ directions depending the solar zenith angle (θ_z). The line of sight of the modelled spectrometer is normal to the *X*-*Y* plane in the $+Z$ direction.

[Fig. 1]

The optical depth (τ) through the dust devil is defined by:

$$\tau = \sigma_{\text{ext}} NL \tag{1}$$

where σ_{ext} is the extinction cross-section of the particles, N is the dust concentration (number of particles / m^{-3}) and L is the path length (m) through the dust devil. The extinction cross-section is the probability of a photon-particle interaction and is analogous to the projected area of the species as seen by the photons. The product $\sigma_{\text{ext}} N$ is defined as the extinction coefficient (k_{ext}) which is a measure of the extinction per unit length (m^{-1}) and is used in the model to describe heterogeneities in the dust distribution.

2.2 Dust scattering and absorption

For each photon-dust particle interaction there is a chance that the photon will either scatter or be absorbed by the dust grain. The probability of an absorption event occurring is governed by ω_0 and is equal to (1- ω_0). For each interaction a random real number between 0 and 1 is generated and absorption occurs if the random number is greater than ω_0, otherwise the photon scatters. Two methods can be used to describe the absorption by dust particles (Whitney, 2011). The first removes the photon from the system if an absorption event occurs, the second incrementally reduces the photon weight by a factor of (1- ω_0). Both methods were applied in the model, though the second method processed scattering events and tracked photons with small weights, significantly increasing the simulation run-time. Owing to computational constraints, long run times were undesirable as this

limited the overall number of photons that could be injected into the model volume, increasing the √N error. The difference in the number of photons detected between the two methods was two orders of magnitude lower than the number of photons detected, therefore the removal method was applied.

If scattering occurs, the angle through which a photon scatters is determined by the phase function of the dust grains. The model has the capability of using both the single and three parameter analytical Henyey-Greenstein phase function (Cashwell and Everett, 1959; Witt, 1977) and phase functions produced by semi-empirical codes used to model spherical particles (Mie theory) and non-spherical particles (T-matrix and Discrete Diploe Approximation, DDA). The expressions provided by Witt (1977) are used to relate the new cosine direction to a uniform random number between 0 and 1. The assumption of randomly orientated dust particles allows one to assume independence between the scattering phase function and the scattering azimuth angle, and thus the scattering azimuth angle is determined by producing a uniform random number between 0 and 2π. The two scattering angles are determined in the particles' reference frame and are transformed to the global frame coordinate system using the equations of transformation defined in Cashwell and Everett (1959).

After each photon–particle interaction, photons remaining in the simulated dust devil are carried forward in the model, with the photon behaviour after subsequent scattering events being simulated by repeating the procedure described above. From here the term *scattering cycle* refers to one pass through the model, i.e. one scattering event. Photons that are outside of the vortex and are travelling parallel or away from the simulated desert floor ($Z = 0$) are removed from the simulation. If the photons are outside the dust devil and travelling toward the desert floor, the interaction point of the line joining the photon along its trajectory and the desert floor is computed before being removed.

2.3 Spatial variation in dust distribution

The equations described in Witt (1977) and Whitney (2011) require the assumption of a uniform dust distribution within the dust devil. However, for intense vortices this is a poor approximation and the majority of the dust is entrained in the 'wall' of the vortex which surrounds a central core of

significantly lower dust concentration (Sinclair, 1973). The non-uniformity in dust concentration (N) was modelled as a concentric ring of high k_{ext} around a central cylinder of lower k_{ext}, with the cylinders being approximated using the integer grid approximation, creating a uniform grid over the model X-Y plane. To find the distance travelled by a photon within the dust devil, knowledge of the cumulative optical depth (τ_c) in front of the photon direction of travel is required. Lookup tables of τ_c relative to the centre of the vortex are generated for an observer looking along the Y-direction (the X-axis could also have been used since the dust devils are assumed symmetrical in the X-Y plane). The generated τ_c lookup table is required to generate a second lookup table relating τ_c to a distance travelled down each grid path.

Relating the distance travelled by the photon in any given direction to an optical depth requires transformation of the photon (X,Y) coordinate and vectors (u_x, u_y, u_z) on to the Cartesian coordinates of the τ_c grid, (X', Y') and (u_x', u_y', u_z'), such that the photon direction vector is parallel to the Y'-axis (i.e. $u_x' = 0$). The transformation is illustrated in Fig. 2 with a photon travelling along vector 1 (dashed line) being equivalent to a photon travelling along vector 2 (solid line). The transformation allows all the photons within the simulation to be placed on a uniform grid for interpolation. The transformation is performed over the individual photon locations and cosines instead of the τ_c grid as this allows simultaneous calculations over many photons, reducing the computation time. The optical depth associated with the (X', Y') position in the τ_c grid is found by interpolating over the τ_c table. The randomly produced optical depth is then added or subtracted from this value depending on the direction of travel (i.e. the sign of u_y'), with the resulting optical depth and Y' position interpolated onto the distance lookup table to find the new position of the photon.

[Fig. 2]

The absolute difference between the photon's new distance and current distance is calculated to find the distance travelled in the X-Y plane and new photon position is calculated by modifying the transformation equations defined by Cashwell and Everett (1959) for the X-Y plane. As $\sin\theta \rightarrow 0$ (i.e.

as the photon direction vector becomes close to vertical) the transformation equations break down and it is assumed that the X and Y positions of the photons are unchanged for small $\sin\theta$ values since ΔX and ΔY tend to zero. The new Z position is determined from $Z = Z_0 + u_z\,\tau_c / k_{ext}$ where k_{ext} is determined by interpolation of the photon position on the k_{ext} lookup table.

2.4 Error analysis of coordinate system transformation

The large numerical arrays used in the model require single numerical precision for the cosine, sine and interpolation due to memory limitations. This resulted in errors in the photon optical free path and final position on the detection plane. To characterise the magnitude of these errors on the final output of the model, the errors at key stages in the model were analysed. Considering the case of no errors, the photon vectors align parallel to the Y'-axis of the τ_c grid after transformation, giving u_x' a value of zero. Hence the original X' position and the new photon position (X_n') in the τ_c grid will be equal. The introduction of errors results in a departure from the perfect case and $X' \neq X_n'$. Fifty batches of 10^7 photons (a practical limitation) were injected into the system and the $\Delta X'$ computed. Of the photons injected 99% experience a $\Delta X' < 1\times10^{-5}$ m with the remaining 1% having an error of 1×10^{-4} m. The impact of the rotation errors on the new (X, Y, Z) coordinates of the photons is small with > 85% of all photon interactions having a ΔX between 1×10^{-4} m and 1×10^{-5} m, and a ΔY between 1×10^{-5} m and 1×10^{-6} m. Approximately 99% of the photons showed a ΔZ less than 1×10^{-4} m. A small fraction of the photon interactions have larger positional differences with approximately 0.6 % and 0.006 % of the interactions exhibiting a ΔZ of 0.001 m and 0.01 m respectively, while one in every two million photons show a ΔZ of approximately 0.1 m. The larger errors are associated with the error due to the calculation of the new directional cosines at small angles and the new Z position calculated with a division by $\sin\theta$. The above analysis illustrates the errors introduced by coordinate transformation are negligible. The $\sqrt{N}$ error for the simulations performed was determined to be 1.0%.

3 Dust devil simulations

In this section idealised dust devils of different τ are modelled to assess what effect the quantity of dust has on the photon propagation. For these simulations the composition of the suspended dust is assumed to be constant, i.e. σ_{ext} is constant. A second set of simulations investigates the effect of different single scattering properties on the photon propagation with N held constant.

3.1 Model parameters

The model requires specification of: solar elevation angle, dust devil height, dust devil radius, location of the point of measurement (PoM), optical properties of the dust entrained in the vortex, the detection plane height (set to the height of the PoM above the surface) and the interpolation lookup tables. Two scenarios are presented; the first assumes the full sky light flux (FS) is measured by the detector (i.e. half-angle Field of View, FoV = 90°) and the second applies a narrow view (NV) such that the solar disc does not enter the detector FoV, meaning that only scattered light is detected. For all simulations in this section, the solar elevation angle was held constant at 76.5°, which corresponds to the maximum solar elevation angle before the solar disc enters the FoV in the NV case, assumed to be 12.7°. The dust particle scattering phase function was described by the Henyey-Greenstein approximation.

3.2 Photon Propagation

The initial positions of the photons for the FS model are found by generating random numbers so that the photons are positioned in the X-Y plane at the height of the dust devil. The NV case resulted in significantly fewer photons being detected since only scattered photons are detected. To increase the photon density, only photons that intersect the vortex are considered. Increasing the number of photons injected into the system was not a practical solution due to the available computing resources. The initial positions of the photons are randomised on the illuminated edge, described as the Sun-facing edge, by randomly selecting $-R_{dd} \leq Y \leq R_{dd}$ and $0 \leq Z \leq Z_{dd}$, The X position is then

determined using Pythagoras' theorem. The photons are propagated forward in the model until all photons are either detected or propagate outside the model volume.

Fig. 3 shows the propagation of the photons in the *X*-*Y* plane after one and four consecutive scattering events for a dust devil with a high *N* in the wall (k_{ext} = 0.5 m^{-1}) and a dust devil with low *N* in the wall (k_{ext} = 0.05 m^{-1}). Both scenarios assumed a dust free core, and the dust devil is assumed to have core and outer radii of 3.0 and 6.0 m respectively. The black dots mark the positions where the active photons interact with a dust particle only (photons which travelled outside the model volume or were detected on the previous cycle are not shown in consecutive figures). The simulations show what effect varying the dust concentration has on the propagation of the photons through the vortex. After the first cycle the high opacity case shows that the majority of the photons will interact with a dust particle close to the inside edge of the illuminated wall or on the inside edge of the non-illuminated wall. In contrast, after one scattering event the dust devil with low *N* in the wall displays a much more uniform distribution with a significantly higher portion of the photons passing directly through without interacting. As more cycles are performed the photons migrate towards the non-illuminated side. However, this process is 'slower' at high *N* as a result of the higher probability of photon–dust particle interaction, with the majority of the photon-dust particle interactions still occurring in the illuminated wall and near the core on the non-illuminated wall after four scattering events. At lower *N* the propagation is more clearly seen and after the same number of scattering events the number of photons present inside the vortex is significantly reduced, with their positions being nearly uniform, albeit with a slight bias towards the non-illuminated edge.

The simulations perform in a physically realistic way. The optical free path of the photons is inversely proportional to k_{ext} and from Eq.(1), with the dust composition constant, is inversely proportional to *N*. Thus as *N* increases the photons will travel a shorter distance before interacting with dust particles. This explains the slower migration of the photons from the illuminated wall to the non-illuminated wall in the high optical depth case compared to the low optical depth scenario.

[Fig. 3]

To illustrate the effect of changes in the scattering nature of the dust particles on the photon propagation, the asymmetry parameter, g, (defined as the average cosine of the scattering angle weighted by the phase function) was assigned values of 0.70, 0.80, 0.90 and 0.98. The NV model was used for a dust devil with $\tau = 0.6$. The position of the photons after six scattering events is shown in Fig. 4 for g = 0.70 and 0.98. As Fig. 4 illustrates, for lower values of g, the location where the photons cross the detector plane is more uniformly spread around the vortex. At high g values, the positions where the photons cross the detector plane are highly concentrated in the $+X$ plane and cover an area only slightly larger than the dust devil radius. This result is expected, since as $g \rightarrow 0$ the photon scattering will tend towards isotropic resulting, in a more uniform distribution of photons around the vortex. As $g \rightarrow 1$ the photons will scatter more favourably in the forward direction and the positions where the photons cross the detector plane will be concentrated on the opposite side ($+X$) from where they enter ($-X$).

[Fig. 4]

4 Simulated dust devil transits

The FS case will detect photons which pass directly through the dust without interaction (direct component) and also any photon scattered onto the PoM (scattered component). The simulations assume a sky free of dust and clouds resulting in the direct component forming the majority of the total surface irradiance and therefore as a dust devil transits[1] across the detector the number of photons detected decreases by a factor of $\exp[-k_{\text{ext}}L]$, where L is the path length through the dust. The scattered component increases during the transit, though the increase is small in comparison to the decrease in the direct component. In contrast, when a dust devil transits in the NV case an increase in

[1] A 'transit' is defined as the passage of a dust devil such that the PoM passes through the low pressure core of the vortex.

detected photons should be observed. This is because the FoV in the NV case precludes detection of the direct component and therefore only the scattered component is detected, which increases as N (hence k_{ext}) increases resulting in a net increase in signal over the ambient signal. Fig. 5 shows the normalised total (Φ_T) and scattered (Φ_S) photon flux over the model surface for both FoV cases for a dust devil with a radius of 2 m and τ = 0.6.

[Fig. 5]

In the following sections a transit of a dust devil moving in the $-X$ direction is simulated for τ of 0.15, 0.3, 0.6, 0.9, 1.2, 1.6 and 2.0. For a uniform dust devil with an outer radius of 2 m this results in k_{ext} of 0.0375, 0.075, 0.15, 0.225, 0.3, 0.4 and 0.5 m^{-1} respectively. Note that since the dust devil size and composition is fixed the quantity being varied is the dust concentration N. For a non–uniform dust devil three scenarios were considered: the first assumes 1/4 of the total dust is in the core with the remainder in the wall. The second and third assume 1/3 and 2/5 of the dust is present in the core leaving 2/3 and 3/5 of the dust in the wall respectively. Table 1 provides k_{ext} for each scenario for a non–uniform dust devil with a core radius of 1 m and the same outer radius as the uniform dust devil.

[Table 1]

4.1 Effect of dust loading

The transit of a dust devil with the parameters of Scenario 1 is used to investigate the effect of increasing dust loads, Fig. 6. From examination of the simulated dust devil transits we would expect a dust devil of high dust loading, for the NV case, to be characterised by a significant increase in the scattered photon flux (Φ_S) as the illuminated edge passes over. This would be followed by a sharp decrease in Φ_S through the core and non–illuminated wall. For high N, Φ_S is approximately 150% and 300% larger in the illuminated wall compared to the dust devil core and non-illuminated wall respectively. Lower dust concentrations result in fewer photon–particle interactions lowering the probability of scattering into the PoM, causing Φ_S in the illuminated wall to decrease. The longer

optical free path for low N allows more photons to penetrate into the core and opposite wall and correspondingly Φ_S in the core and non-illuminated wall increases. For vortices with τ of 0.15 and 0.3, the optical free path far exceeds the diameter of the dust devil and as a result Φ_S quickly decreases, with ~70% less flux detected in the core for a dust devil with τ = 0.15 compared to vortices with τ = 0.6. At these low dust concentrations the internal distribution of the dust becomes important and the uniform case shows a peak in Φ_S at the dust devil centre while the more heterogeneous dust devils (Scenario 1) show small maxima in flux near the core–wall boundary of the illuminated and non-illuminated wall and less scattered light detected at the dust devil core.

[Fig. 6]

The total photon flux (Φ_T) transit signatures can generally be characterised by a reduction in Φ_T as the vortex passes over the PoM. Closer examination of the transits reveals that above a k_{ext} of 0.24 m^{-1} in the dust devil wall there is an increase in Φ_T as the dust devil approaches the PoM. A peak flux is observed just inside the illuminated wall, X = -1.8 m, with the high opacity dust devils showing a 10% increase in Φ_T. The higher Φ_T is a result of the increase in Φ_S being larger than the decrease in the direct light flux at X = 1.8 m leading to a net increase in Φ_T. Further into the vortex Φ_T decreases depending on τ, with low τ showing a more gradual decline between X = -1.8 m and X = 1.0 m compared to high dust optical depths (τ = 2.0). As the PoM passes through the core a slight change in the gradient is observed at high dust concentrations in the heterogeneous dust devils, which is not observed in the uniform case. Upon exiting the dust devil the gradient reduces significantly and Φ_T reduces gradually to a minimum at $X \approx$ 14.0 m before increasing back to the ambient flux. This result is significant as it shows that for dust devil transits with this geometry (vortices moving directly towards or away from the Sun) the position of lowest measured flux does not correlate with the portion of the transit signature associated with the dust devil interior but to the location on the surface where the optical depth along the photon incident path is at a maximum. This occurs at the point where the line joining the PoM to the Sun has the longest path length through the dust devil.

[Fig. 7]

4.2 Effect of dust distribution

To determine the effect of the different internal dust distributions on the transit signature the observed Φ_S in the core and non–illuminated wall relative to the illuminated wall was plotted as a function of dust devil uniformity, which is defined as the ratio of the core dust concentration to the dust concentration present in the walls, (N_c / N_w). Fig. 8 shows that for low dust concentrations, Φ_S in the dust devil core is strongly dependent on the internal dust distribution. A dust devil with τ = 0.15 and a core dust concentration 1/3 of the wall experiences an increased Φ_S of ~35 % in the core relative to the illuminated wall. As the dust devil becomes more uniform the relative scattered flux in the core increases, with almost twice the scattered photon flux observed relative to the illuminated wall for the uniform case. At τ = 1.2 the dust concentration in the dust devil walls for Scenario 1 and 2 results in the optical free path of the photons being less than the width of the walls resulting in Scenario 1 and 2 experiencing a decrease in Φ_S of ~10% and 2% respectively relative to the illuminated wall. Dust distributions with a higher degree of homogeneity (Scenario 3 and the uniform case) predict 2% and 16% increase in Φ_S entering the PoM at the core than in the illuminated wall. This indicates that the different internal dust distributions will result in very different transit signature, with Scenario 1 and 2 showing an increase in Φ_S in the illuminated wall over the core while the more uniform dust devils predict a lower Φ_S in the illuminated wall relative to the core. As the dust concentration increases heterogeneities in the internal dust distribution become less important. At τ = 2.0, Scenario 1 and the uniform case predict ~40% and ~30% less scattered flux in the core respectively. The scattered photon flux in the non–illuminated wall relative to the illuminated wall showed little dependence on the internal dust distribution with the relative scattered flux constant or all internal dust distributions considered.

The FS simulations showed that Φ_T in the core and non-illuminated wall relative to Φ_T in the illuminated wall to be approximately constant for all τ cases. This indicates the internal dust

distribution will have an almost negligible effect on the spectral signature of a dust devil transit when measuring Φ_T. The driving parameter governing the transit signature shape is the total amount of dust along the line joining the source to the detector. From the Beer-Lambert law the direct flux is a function of τ for a fixed θ_z. Therefore the manner in which the dust is distributed with the dust devil will have no impact on the direct component if τ is fixed and the slight variations in the FS transit signatures are due only to the scattered component. This correlates with the assumption that the direct component forms the majority of the total surface flux during 'clear sky' conditions.

[Fig.8]

4.3 Effect of core size

To investigate different internal structures the dust devil core radius (R_{core}) was varied to be 1/4, 1/2 and 3/4 of R_{dd} to determine the effect of different core and wall thickness on Φ_S. This corresponds to core radii of 0.5, 1.0 and 1.5 m respectively for a dust devil with an outer radius of 2 m. The dust distribution defined in Scenario 2 was applied to dust devils with τ of 0.6 and 1.2.

The NV transits, Fig. 9, reveal that Φ_S is highly dependent on the vortex core size. Since the quantity of dust in the two regions is held constant as the core volume is increased, N in the wall is enhanced while the core sees a reduction in N. Reducing the core diameter has the opposite effect, increasing the wall and decreasing the core volume, hence lowering and enhancing the dust concentration in two regions respectively. Looking at the transit of a dust devil with a core radius of 1.5 m and dust loading, τ = 1.2, the signature shows a significant departure compared to the R_{core} = 1.0 m case and more closely resembles a high optical depth dust devil with a core and outer radius of 1.0 m and 2.0 m, Fig. 6. This is because the dust concentrations in the wall of the two dust devils lead to a similar k_{ext} of 0.8 m^{-1} and 0.67 m^{-1}. At τ = 0.6 the increased dust concentration in the wall results in a broadening of the uniform flux within the dust devil interior and the appearance of two peaks in Φ_S at the outer edge of the illuminated and non–illuminated walls. For both dust optical

depths the transit signature of a dust devil with a small central core will be characterised by a peak in intensity at the dust devil centre similar to the transit by a uniform dust devil.

[Fig. 9]

The simulated transits show that Φ_S is strongly dependent on N in the vortex wall which is a function of τ, dust devil size, core diameter and also the internal dust distribution. Therefore, if both τ and the dust devil size are known, the transit signature will be able to give insight not only into the internal structure and dust distribution, but more importantly the dust concentration. For example, a large Φ_S in the illuminated wall relative to the core is characteristic of a dust devil with a high N in the vortex wall. This can be a result of a dust devil with a moderate dust loading but large internal core resulting in a low wall volume or by a vortex with a high dust loading and a smaller core but with the majority of the dust contained within the wall. If Φ_S is approximately uniform during the dust devil transit, this is an indication of low N throughout the vortex.

4.4 Effect of transit trajectory

The scattered and total photon flux over the NV and FS model surfaces, Fig. 5, can be used to determine the transit signature for any dust devil trajectory over the PoM by interpolating over this model surface. The trajectory of the dust devil is defined here as the angle (α_{dd}) at which the PoM enters the vortex relative to the illuminated edge. A number of simulated dust devil transits were performed using different trajectories to investigate the effect on the Φ_S and Φ_T transit signatures and the results are shown in Fig. 10. All simulations in this section apply to a dust devil with R_{core} = 1 m and outer radius of 2 m with k_{ext} of 0.1 m^{-1} and 0.4 m^{-1} in the core and wall respectively. As illustrated for the NV case, the direction of travel over the PoM relative to the illuminated side can result in a significantly different transit signature, especially for high N in the dust devil wall. The transit signatures show Φ_S will be greatest if the PoM passes through the illuminated wall; therefore if the dust devil is moving away from the Sun (α_{dd} =180°) and the PoM enters from the non-illuminated

side, the peak Φ_S will be observed in the trailing wall (i.e. after the decrease in pressure at the core). Alternatively if the dust devil is heading towards the Sun ($\alpha_{dd} = 0°$) the leading edge wall will experience a higher Φ_S. As $\alpha_{dd} \rightarrow 90°$, Φ_S in the illuminated wall will decrease while Φ_S in the non-illuminated wall increases, leading to a constant Φ_S through the vortex interior at $\alpha_{dd} = 90°$.

The FS model shows total flux transit signature is significantly modified by the trajectory of the dust devil over the PoM. At increased angles from the illuminated wall, the path length through the dust devil shadow decreases resulting in a reduction of the transit signature width. This leads to the location where Φ_T is smallest to migrate towards the dust devil interior. A perpendicular transit of a non–uniform dust devil is characterised by the point of lowest flux coinciding with the core–ward edge of the leading and trailing walls and an increase in flux at the dust devil core. It should be noted that the high symmetry of the perpendicular transit is an artefact of the *X*-*Y* plane symmetry assumed in the model and such symmetry is unlikely to be measured in reality. The transit signature for dust devils with trajectories such that the PoM enters the non-illuminated side of the dust devil will be the reverse of the transits shown in Fig. 10.

[Fig. 10]

4.5 Effect of single scattering properties

The optical properties of the dust particles entrained in the dust devil were varied to assess the sensitivity of the model to changes in the single scattering properties. Fig. 11 shows a dust devil transit for both the NV and FS cases for changes in the asymmetry parameter (with $\omega_0 = 0.95$ and the scattering phase function of the dust particle described by a Henyey-Greenstein phase function). A transit parallel and perpendicular to the *X*-axis is assumed for the NV and FS cases respectively. The FS case shows that Φ_T increases as $g \rightarrow 1$, whereas, a decrease in Φ_S is observed for the NV case. The different dependence on *g* can be explained by the scattering phase function; at high values of *g* the photons are scattered predominately at forward angles, therefore even though the photon has been scattered it will still be in the direct path to the PoM, and hence will be detected. As *g* decreases the probability of scattering away from the forward direction and out of the direct path increases, this results in fewer photons being detected, hence less light. The reverse is true for the NV case where the photons must be scattered out of the direct path in order to be detected which has a lower probability of occurring at high *g* values. For the NV case, Fig. 11a also reveals that as *g* increases the measured scattered component in the non-illuminated side relative to the core increases. This is a result of more photons penetrating through to the non-illuminated side due to the higher probability of scattering at small angles. Similarly the opposite is true for the illuminated wall, where a decrease in Φ_S is observed for increased values of *g*.

[Fig. 11]

Unexpectedly, for the NV case, the maximum Φ_S does not correspond to the minimum value of *g* but occurs at $g = 0.73$. This can be explained by examining the effect increasing *g* has on the scattering phase function. For a θ_z of 13.5° a photon needs to be scattered by an angle between approximately 5° and 30° in order to be detected given a field of view of 12.7°. The probability of scattering between these values decreases as $g \rightarrow 1$, as the favourable scattering angle approaches 0°.

The maximum scattered flux occurs with $g = 0.73$, as it provides the photons the highest probability of scattering between 5° and 30°.

This indicates a bias effect associated with θ_z on the observed scattered flux for a given g value. At larger or smaller θ_z, the angle through which the photons must be scattered in order to be detected will increase and decrease respectively. The implication is that as the Sun moves towards zenith the g value associated with the peak scattered component will increase as θ_z decreases, since the angle through which the photons must be scattered in order to be detected approaches 0°. Conversely, as the Sun sinks towards the horizon the g value will decrease accordingly. The bias effect is not observed in the FS case as a result of the direct component forming the majority of the light flux and reveals that the bias is limited to the scattered component. This bias is important when interpreting data from potential observations and care is needed when attempting retrieval of the dust optical properties.

The same transit was simulated for changes in ω_0, with g held constant at a value of 0.8, Fig. 12. Both the NV and FS simulations predict that smaller values of ω_0 will result in lower total and scattered fluxes and correlates with a high attenuating dust component absorbing a larger portion of the incident light. At higher values of ω_0 the dust grains are less absorbing and more light is scattered, increasing the probability of detection, and correlates with a higher Φ_S and Φ_T.

[Fig. 12]

5 Conclusion

The spectral variation of sunlight during a dust devil transit was investigated to determine whether the dust load, size and internal structure of the vortex could be estimated from a dust devil transit signature. This work has shown that the spectral signature of a transiting dust devil is highly dependent on the method of observation, with the narrow field of view (NV, assuming the Sun is not in the FoV) and full sky flux (FS) simulations showing contrasting spectral signatures.

In the FS case, Φ_T decreases during the transit since the loss of light from the direct component, as a result of absorption and scattering by the dust particles, is much larger than the gain from increased diffuse scattering. Predictions of Φ_T transit signature revealed a negligible dependence on the dust concentration and core size. This is due to the dominance of the direct component in the total irradiance at the surface under 'clear sky' conditions and therefore, Φ_T is dependent upon the total extinction along the line of sight to the Sun.

In the NV case, the incident solar flux interacts with the dust column of the dust devil vortex resulting in light, which would otherwise be undetected, being scattered into the point of measurement (PoM). This causes the measured flux to increase during a dust devil transit. The NV simulations have shown that Φ_S inside a dust devil vortex is strongly dependent on the dust distribution within the dust devil interior. The Φ_S dependence on the dust concentration manifests itself in the transit signature as a reduction in Φ_S in the region of lower dust concentration and an increase in Φ_S through regions of higher dust concentration. Investigations of terrestrial dust devils have revealed central cores that are relatively free of dust particles (Sinclair, 1974). The NV simulations have shown that this dust free core becomes clearly defined in the Φ_S transit signature as a reduction in Φ_S, enclosed by regions of increased Φ_S as the PoM passes through the vortex. Therefore, by measuring the Φ_S signature of a transiting dust devil, the vortex core dimensions can be quantified, providing a more accurate determination of the dust column volume. Furthermore, measurement of both Φ_T and Φ_S allows determination of the direct flux, from which the dust optical depth can be calculated. Therefore if the

dust particle size distribution and optical properties are known, estimation of the mass concentration and the total mass of dust particulates injected into the atmosphere can be determined. This will result in varying levels of direct solar heating of the atmosphere, dependent on the optical properties of the dust.

The implication of this work is that separate measurement of both the total *and* scattered flux of light is crucial for characterising the distribution of dust within a dust devil by its spectral transit signature. The total light flux observed provides information about the dust devil size and total amount of dust, while the scattered light flux gives details of the internal structure of the vortex. Variation in the dust particle single scattering properties were shown to significantly modify the amount of total and scattered flux detected during the transit. These variations imply that the spectral signature of a dust devil transit will differ depending on the wavelength of observation and the properties of the suspended dust. Therefore by comparing the amount of scattered and total flux received during the transit at different wavelengths it is possible to determine single scattering properties of the dust. Following the simulations presented here, the model could be validated by measuring terrestrial dust devil transits with visible spectrometers covering a spectral range of 300–800 nm.

Our methods could also be applied to laboratory generated dust devil vortices. Measuring the light flux at different locations within laboratory generated dust devils and comparing these results with those predicted by the model would allow determination of the internal structure of such laboratory generated vortices, hence showing whether they are representative of real dust devils. These measurements would also help configure the field work setup for future dust devil observations and assist in the analysis of the measured transit signatures by allowing comparisons of different vortex trajectories over the detector.

Finally we conclude that *in situ* measurements of the spectral signatures of transiting dust devils provide a powerful tool to characterise dust devils, including those on Mars, allowing for

determination of their size, dust concentration, internal structure and dust distribution. The nature of such measurements makes them an ideal technique to use on Mars, only requiring two upward viewing spectrometers of low complexity and mass. Measuring the wavelength dependent transit signatures of dust devils would allow estimation of the total amount of dust lofted into the atmosphere and its radiative properties, which is vital in determining the radiative effect of dust devils on the martian atmosphere.

Acknowledgements

The authors acknowledge STFC for funding this work as part of on-going research (MRP and SRL) and as part of a PhD project (JPM). The authors also express their gratitude to the two anonymous referees for their constructive comments and careful reviews.

References

Alpert, P., *et al.*, 1998. Quantification of dust-forced heating of the lower troposphere. Nature. 395**,** 367-370.

Balme, M., Greeley, R., 2006. Dust devils on Earth and Mars. Reviews of Geophysics. 44.

Balme, M. R., Whelley, P. L., Greeley, R., 2003. Mars: dust devil track survey in Argyre Planitia and Hellas Basin. J. Geophys. Res. 108.

Cantor, B. A., Kanak, K. M., Edgett, K. S., 2006. Mars Orbiter Camera observations of Martian dust devils and their tracks (September 1997 to January 2006) and evaluation of theoretical vortex models. J. Geophys. Res. 111**,** E12002.

Cashwell, E. D., Everett, C. J., 1959. A practical manual on the Monte Carlo method for random walk problems. Pergamon Press.

Deepak, A., Gerber, H. E., 1983. Report of WMO (CAS)/Radiation Commission of IAMAP Meeting of Experts on Aerosols and Their Climatic Effects,(Williamsburg, Virginia, USA, 28-30 March, 1983). Geneva: World Meteorological Organization.

Dubovik, O., *et al.*, 2000. Accuracy assessments of aerosol optical properties retrieved from AERONET sun and sky-radiance measurements. J. Geophys. Res. 105**,** 9791-9806.

Ellehoj, M. D., *et al.*, 2010. Convective vortices and dust devils at the Phoenix Mars mission landing site. J. Geophys. Res. 115**,** E00E16.

Ferri, F., Smith, P. H., Lemmon, M., Rennó, N. O., 2003. Dust devils as observed by Mars Pathfinder. J. Geophys. Res. 108**,** 1–7.

Fisher, J. A., *et al.*, 2005. A survey of Martian dust devil activity using Mars Global Surveyor Mars Orbiter Camera images. J. Geophys. Res. 110.

Fouquart, Y., *et al.*, 1987. Observations of Saharan aerosols: Results of ECLATS field experiment. Part II: Broadband radiative characteristics of the aerosols and vertical radiative flux divergence. Journal of Applied Meteorology. 26**,** 38-52.

Greeley, R., *et al.*, 2003. Martian dust devils: Laboratory simulations of particle threshold. J. Geophys. Res. 108.

Greeley, R., *et al.*, 2010. Gusev Crater, Mars: Observations of three dust devil seasons. J. Geophys. Res. 115**,** E00F02.

Greeley, R., *et al.*, 2006. Active dust devils in Gusev crater, Mars: observations from the Mars exploration rover spirit. J. Geophys. Res. 111**,** E12S09.

Hansen, J., Sato, M., Ruedy, R., 1997. Radiative forcing and climate response. J. Geophys. Res. 102**,** 6831-6864.

Hess, M., Koepke, P., Schult, I., 1998. Optical properties of aerosols and clouds: The software package OPAC. Bull. Amer. Meteor. Soc. 79**,** 831-844.

Ives, R. L., 1947. Behavior of dust devils. Bull. Amer. Meteor. Soc. 28**,** 168-174.

Kaufman, Y. J., Tanré, D., Dubovik, O., Karnieli, A., Remer, L. A., 2001a. Absorption of sunlight by dust as inferred from satellite and ground-based remote sensing. Geophys Res Lett. 28**,** 1479-1482.

Kaufman, Y. J., Tanré, D., Dubovik, O., Karnieli, A., Remer, L. A., 2001b. Absorption of sunlight by dust as inferred from satellite and ground-based remote sensing. Geophysical Research Letters. 28**,** 1479-1482.

Levin, Z., Joseph, J. H., Mekler, Y., 1980. Properties of Sharav (Khamsin) dust-Comparison of optical and direct sampling data. Journal of Atmospheric Sciences. 37**,** 882-891.

Metzger, S. M., Dust devils as Aeolian Transport Mechanisms in Southern Nevada and the Mars Pathfinder Landing Site, Ph.D. dissertation**,** pp 236. University of Nevada, 1999a.

Metzger, S. M., Carr, J. R., Johnson, J. R., Parker, T. J., Lemmon, M. T., 1999b. Dust devil vortices seen by the Mars Pathfinder camera. Geophys Res Lett. 26**,** 2781-2784.

Neakrase, L. D. V., Greeley, R., 2010a. Dust devil sediment flux on Earth and Mars: Laboratory simulations. Icarus. 206**,** 306-318.

Neakrase, L. D. V., Greeley, R., 2010b. Dust devils in the laboratory: Effect of surface roughness on vortex dynamics. J. Geophys. Res. 115**,** E05003.

Neakrase, L. D. V., Greeley, R., Iversen, J. D., Balme, M. R., Eddlemon, E. E., 2006. Dust flux within dust devils: Preliminary laboratory simulations. Geophysical research letters. 33**,** L19S09.

Rennó, N. O., Burkett, M. L., Larkin, M. P., 1998. A simple thermodynamical theory for dust devils. Journal of the atmospheric sciences. 55**,** 3244-3252.

Ryan, J. A., Carroll, J. J., 1970. Dust devil wind velocities: Mature state. J. Geophys. Res. 75**,** 531-541.

Ryan, J. A., Lucich, R. D., 1983. Possible dust devils, vortices on Mars. Journal of geophysical research. 88**,** 11005-11,011.

Shettle, E. P., Fenn, R. W., Models of the atmospheric aerosols and their optical properties. Vol. 1, 1976.

Sinclair, P. C., A Quantitative analysis of the dust devil, Ph.D. dissertation**,** pp 292. University of Arizona, 1966.

Sinclair, P. C., 1973. The lower structure of dust devils. Journal of Atmospheric Sciences. 30**,** 1599-1619.

Sinclair, P. C., Vertical transport of desert particulates by dust devils and clear thermals. California Univ., Livermore (USA). Lawrence Livermore Lab., 1974.

Thomas, P., Gierasch, P. J., 1985. Dust devils on Mars. Science. 230**,** 175.

Vincendon, M., Langevin, Y., 2010. A spherical Monte-Carlo model of aerosols: Validation and first applications to Mars and Titan. Icarus. 207**,** 923-931.

Whelley, P. L., Greeley, R., 2006. Latitudinal dependency in dust devil activity on Mars. Journal of geophysical research. 111**,** E10003.

Whitney, B. A., 2011. Monte Carlo radiative transfer. Arxiv preprint arXiv:1104.4990.

Witt, A. N., 1977. Multiple scattering in reflection nebulae. I. A Monte Carlo approach. Astrophys. J., Suppl. Ser.;(United States). 35.

Fig. 1. Global coordinate system of the model volume, (X_0, Y_0) is defined as the centre of the dust devil. Also shown is the decomposition of the photon vector $\mathbf{P}_v$ in to its direction cosines.

Fig. 2. Rotation of a photon vector onto the optical depth grid.

Fig. 3 The photon positions after one scattering event in a dust devil of (a) high and (b) low dust concentration, and after four scattering events, (c) high and (d) low dust concentration.

Fig. 4. Photon positions after six scattering events for: (a) g = 0.7and (b) g = 0.98.

Fig. 5. The photon flux during a transit of a 2 m diameter dust devil with τ = 0.6 for: (a) NV case and (b) FS case.

Fig. 6. NV dust devil transits from Scenario 1 (black lines) and uniform Scenario (grey lines) for different cumulative optical depths.

Fig. 7. As fig.6, but showing the FS simulated transits.

Fig. 8. The observed scattered photon flux in the core relative to the illuminated wall as a function of N_c / N_w.

Fig. 9. The transit signature of dust devils with core radii of 0.5, 1.0 and 1.5 m. The internal dust distribution from scenario 2 is used and the dust devils have dust optical depths of 0.6 and 1.2.

Fig. 10. The variation in the dust devil transit signature for different trajectories over the PoM: (a) NV model (b) FS model.

Fig. 11. Transit of a dust devil moving along the *X*-axis for different asymmetry parameter values with ω_0 held constant at 0.95 (a) NV model, (b) FS model.

Fig. 12. Transit of a dust devil moving along the *X*-axis for different ω_0 values with g held constant at 0.8: (a) NV model and (b) FS model.

Table 1: k_{ext} in the core and walls for non-uniform dust devils under the different scenarios considered for each τ.

Figure 1

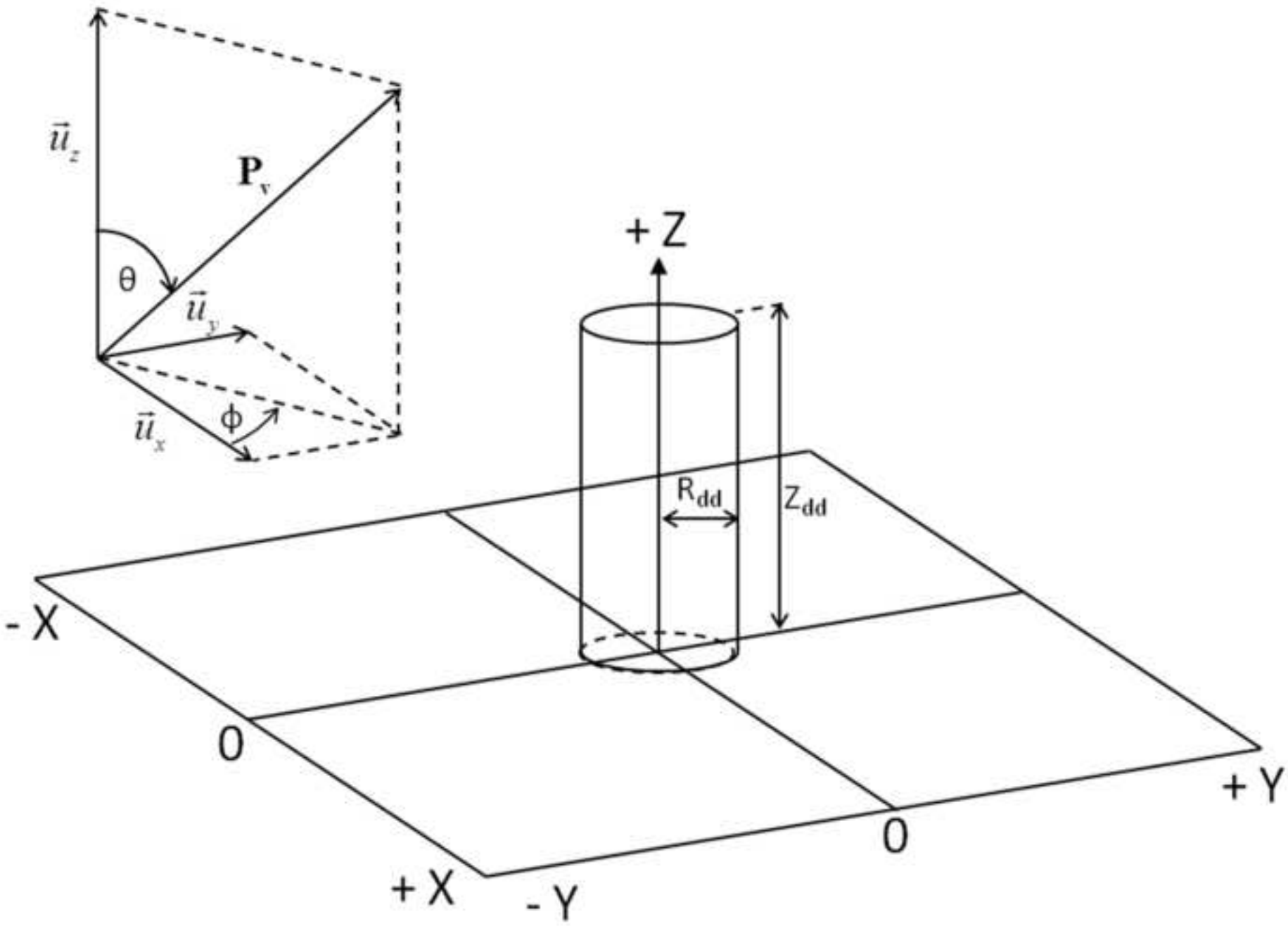

Figure 2

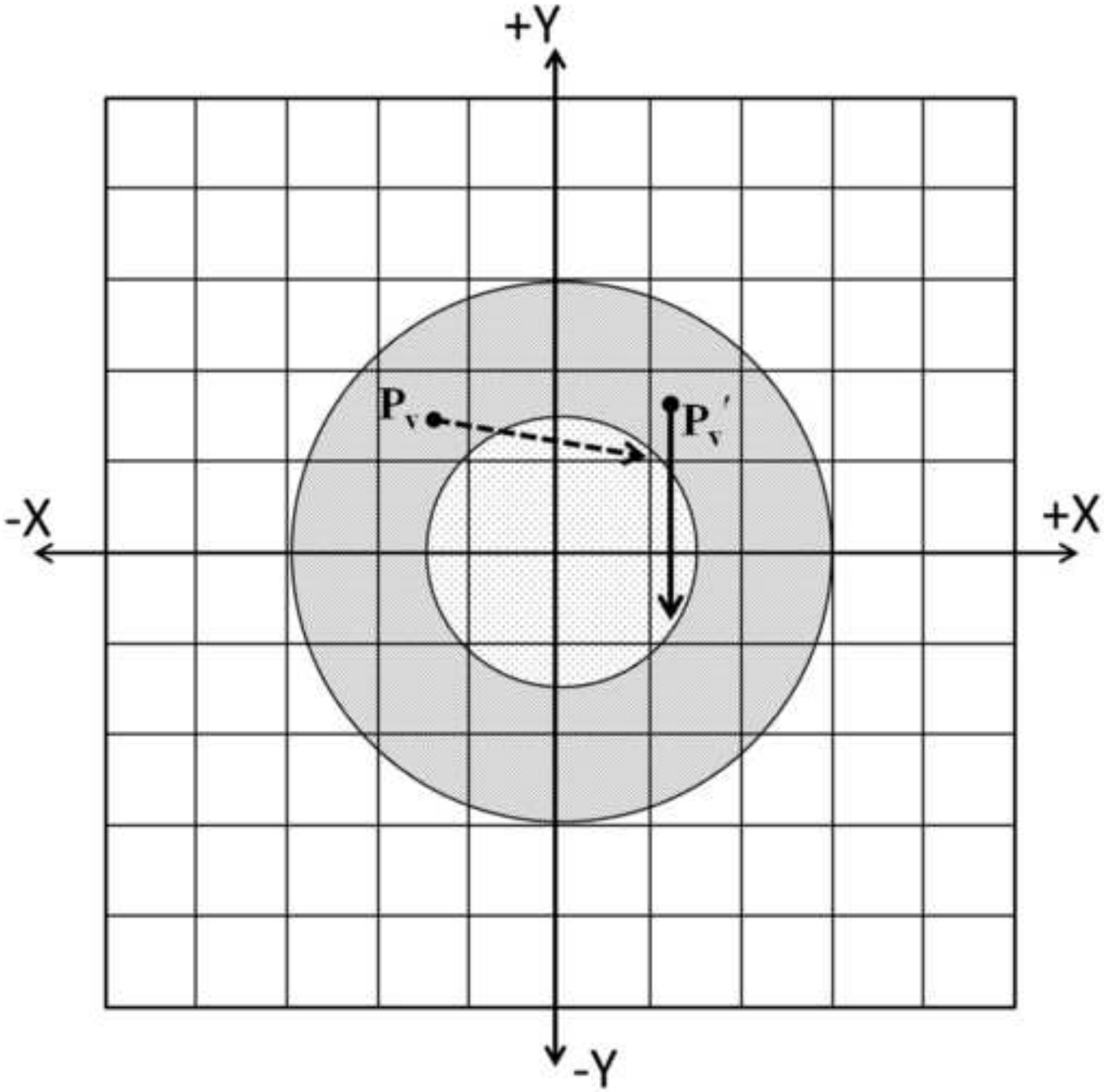

Figure 3

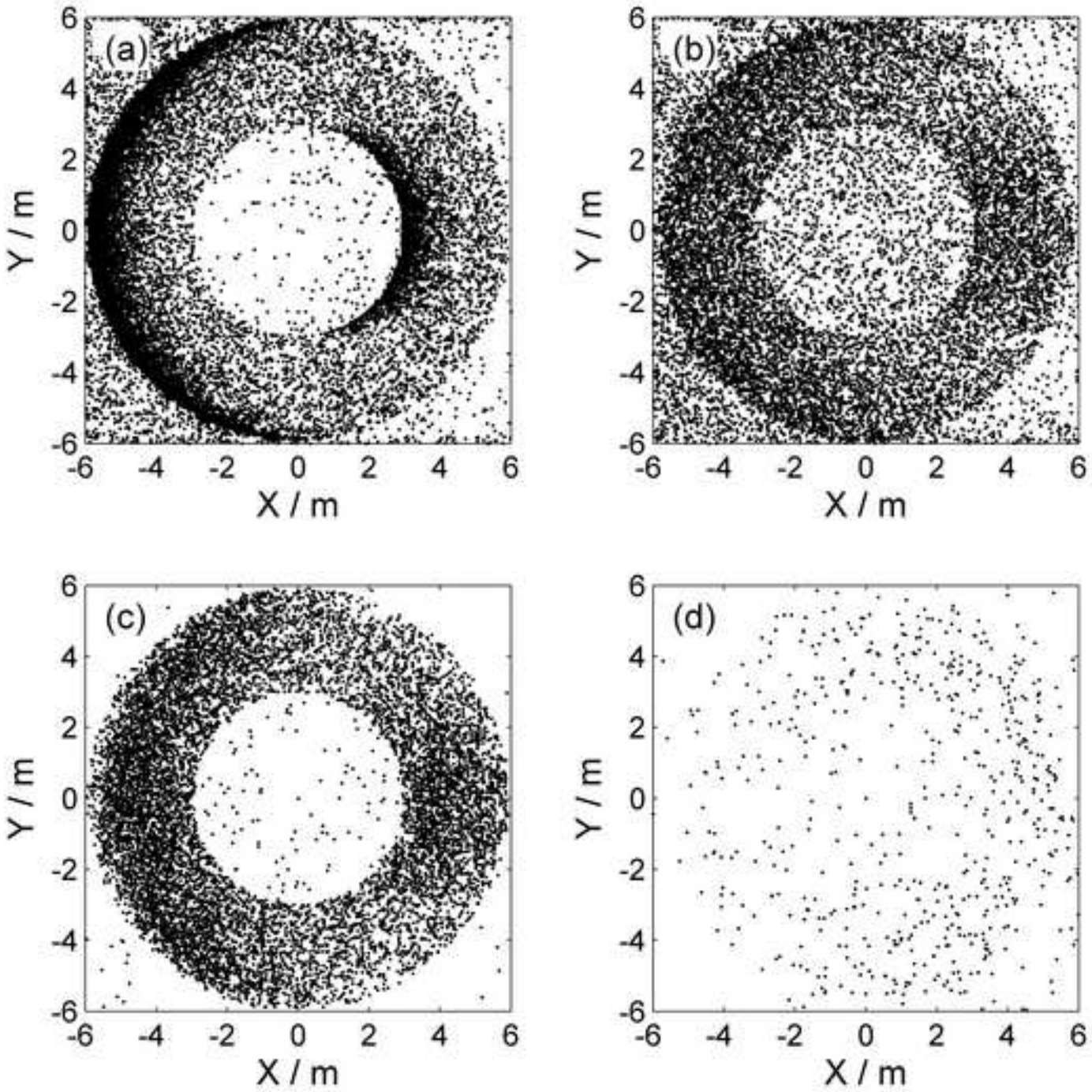

Figure 4

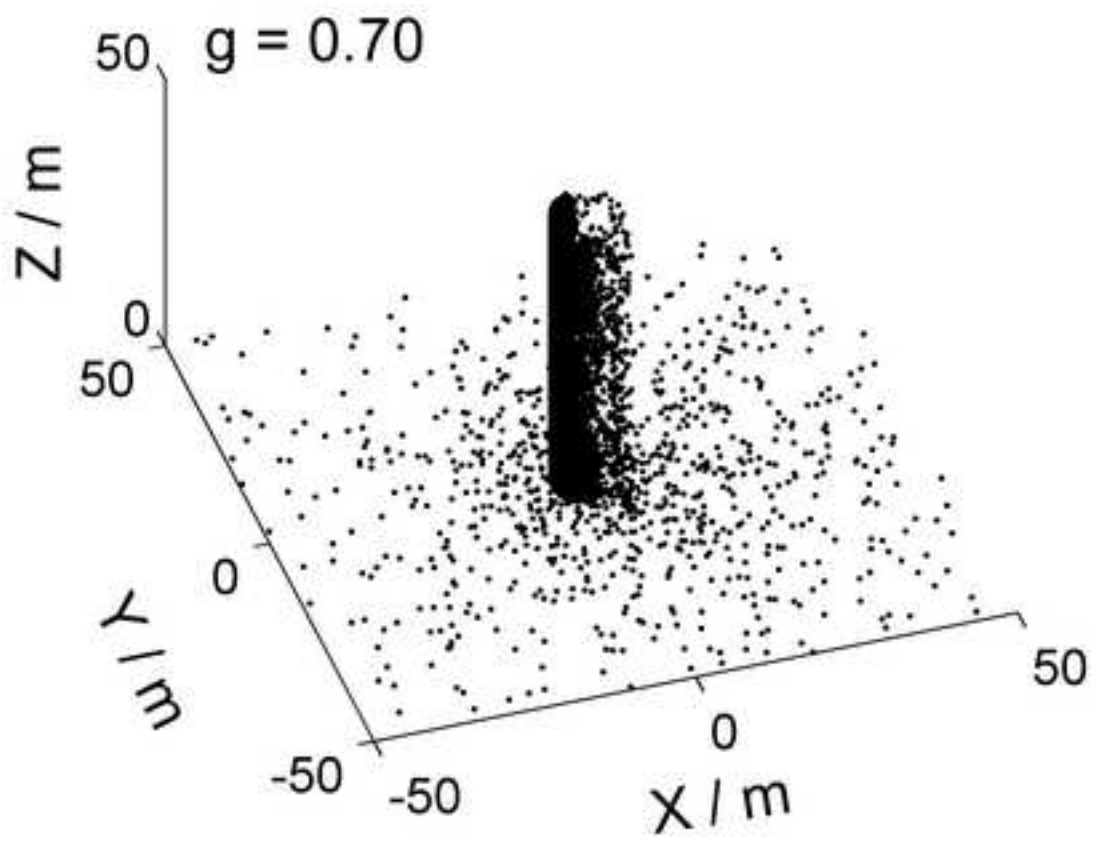

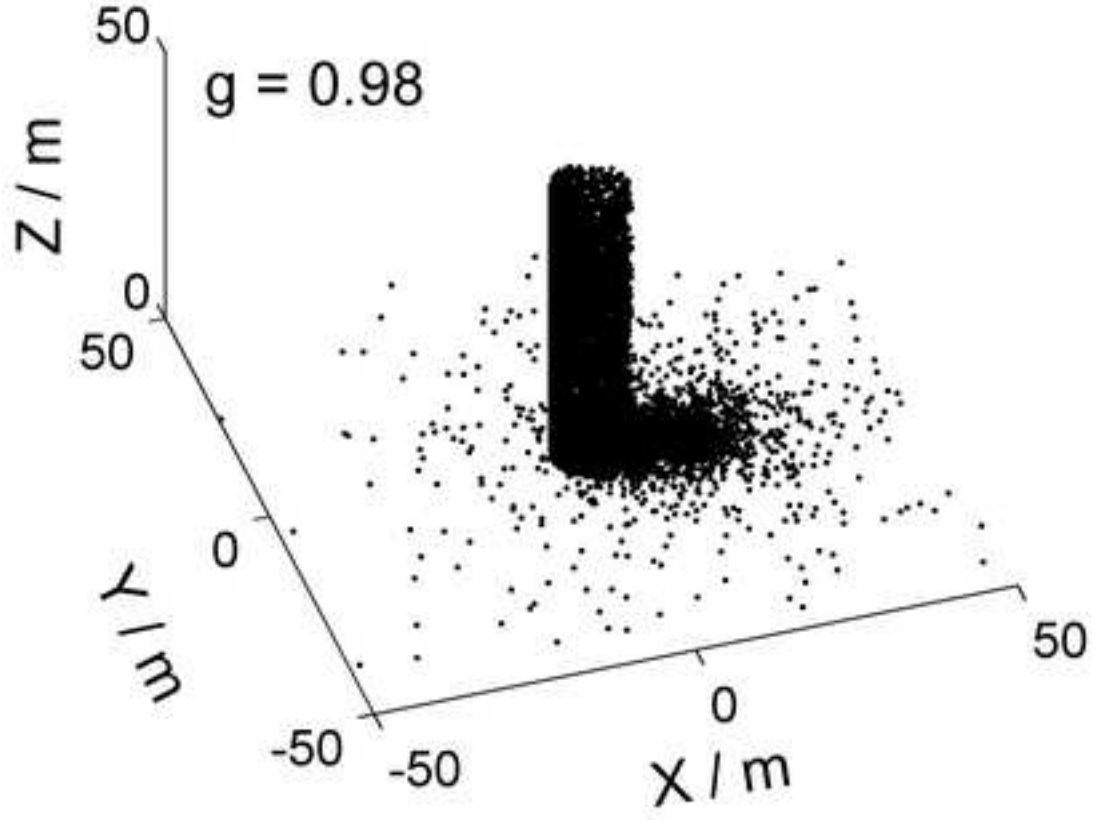

Figure 5

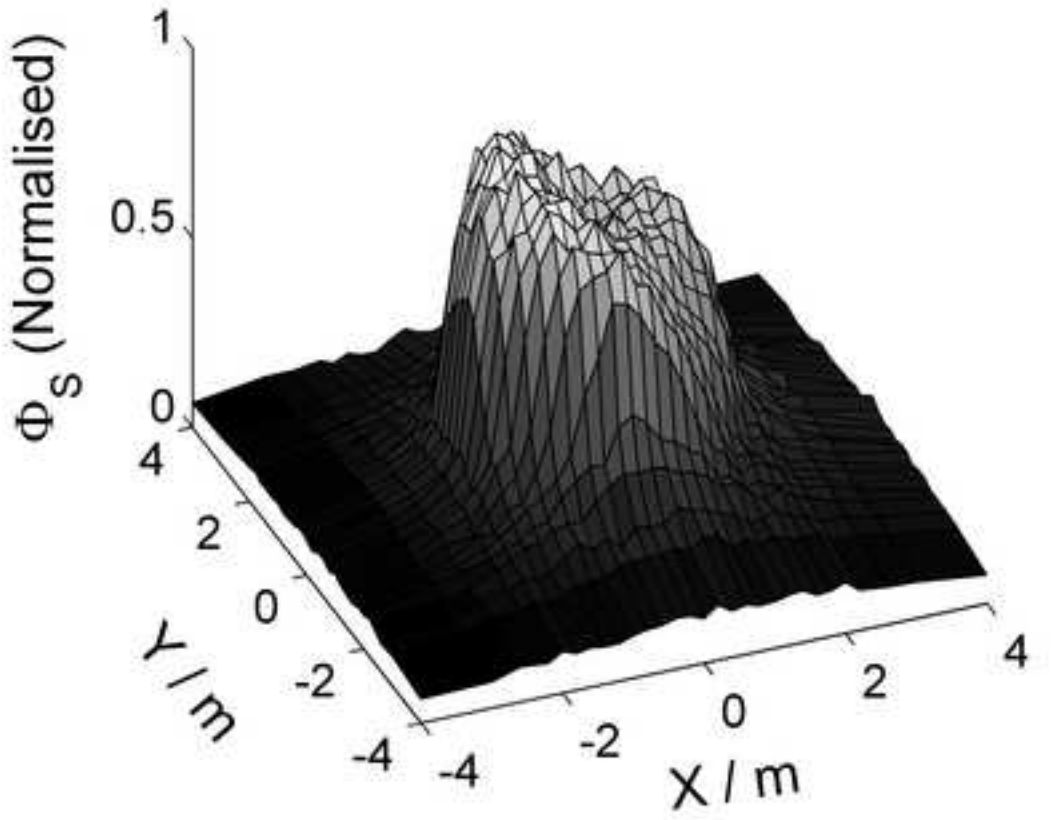

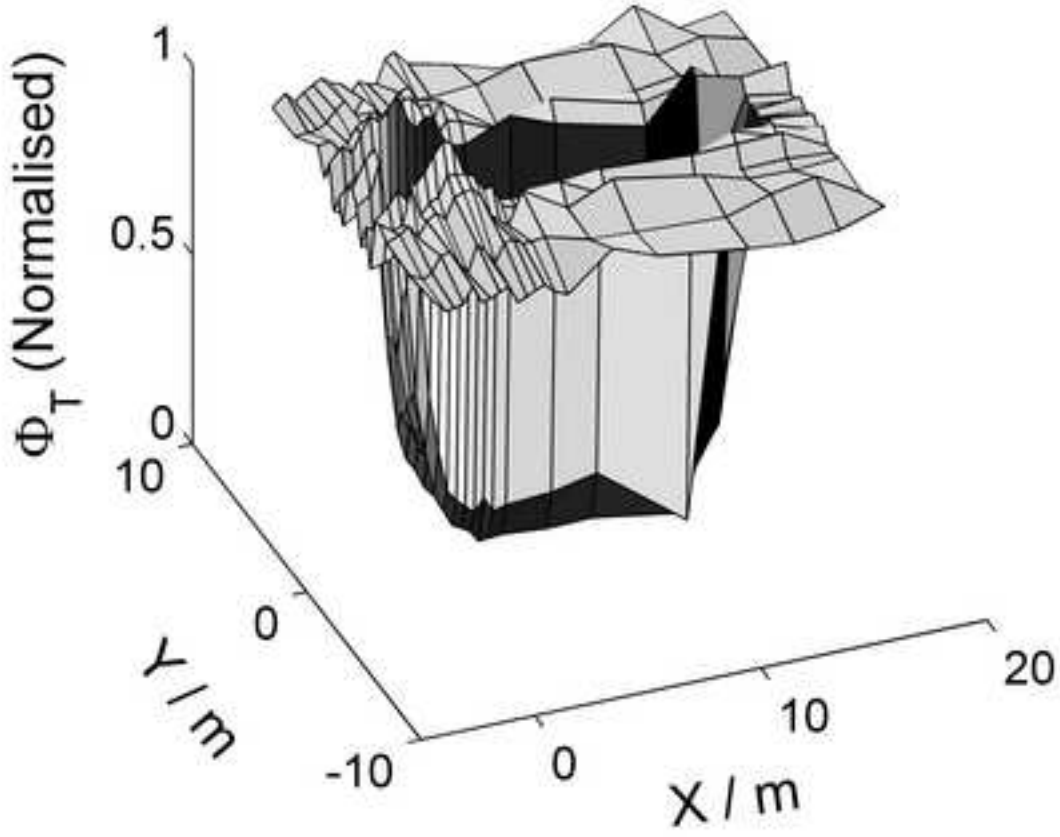

Figure 6

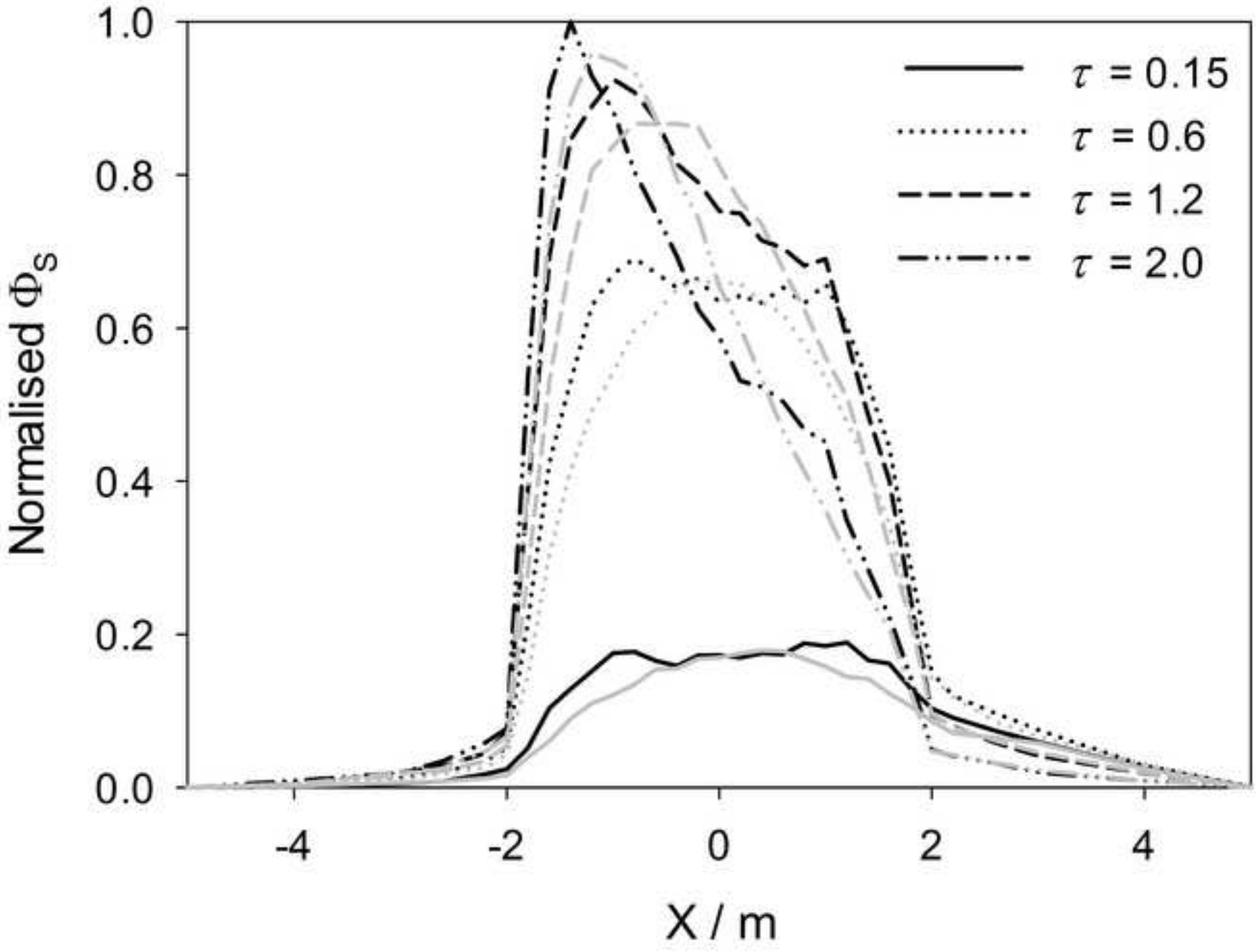

Figure 7

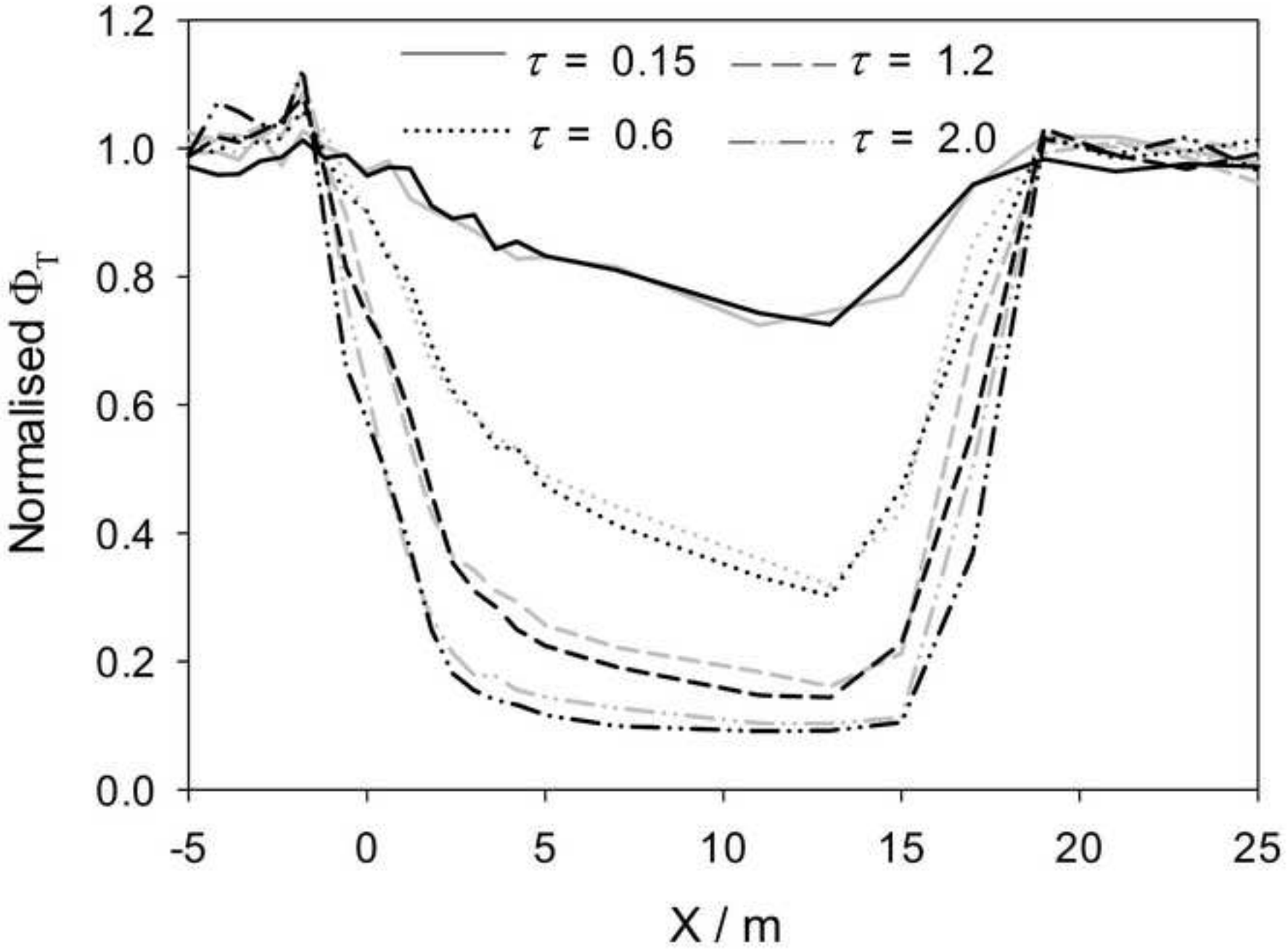

Figure 8

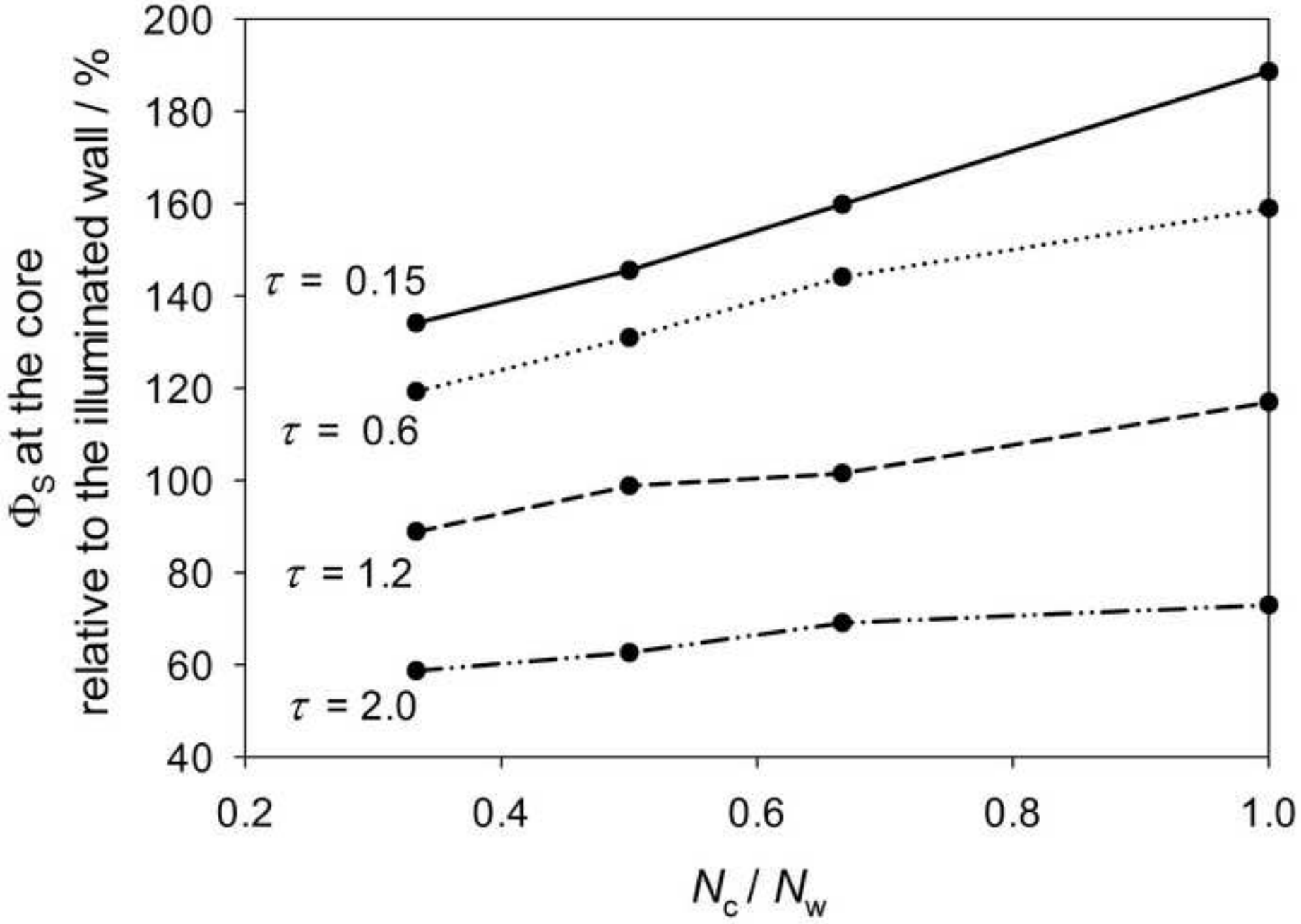

Figure 9

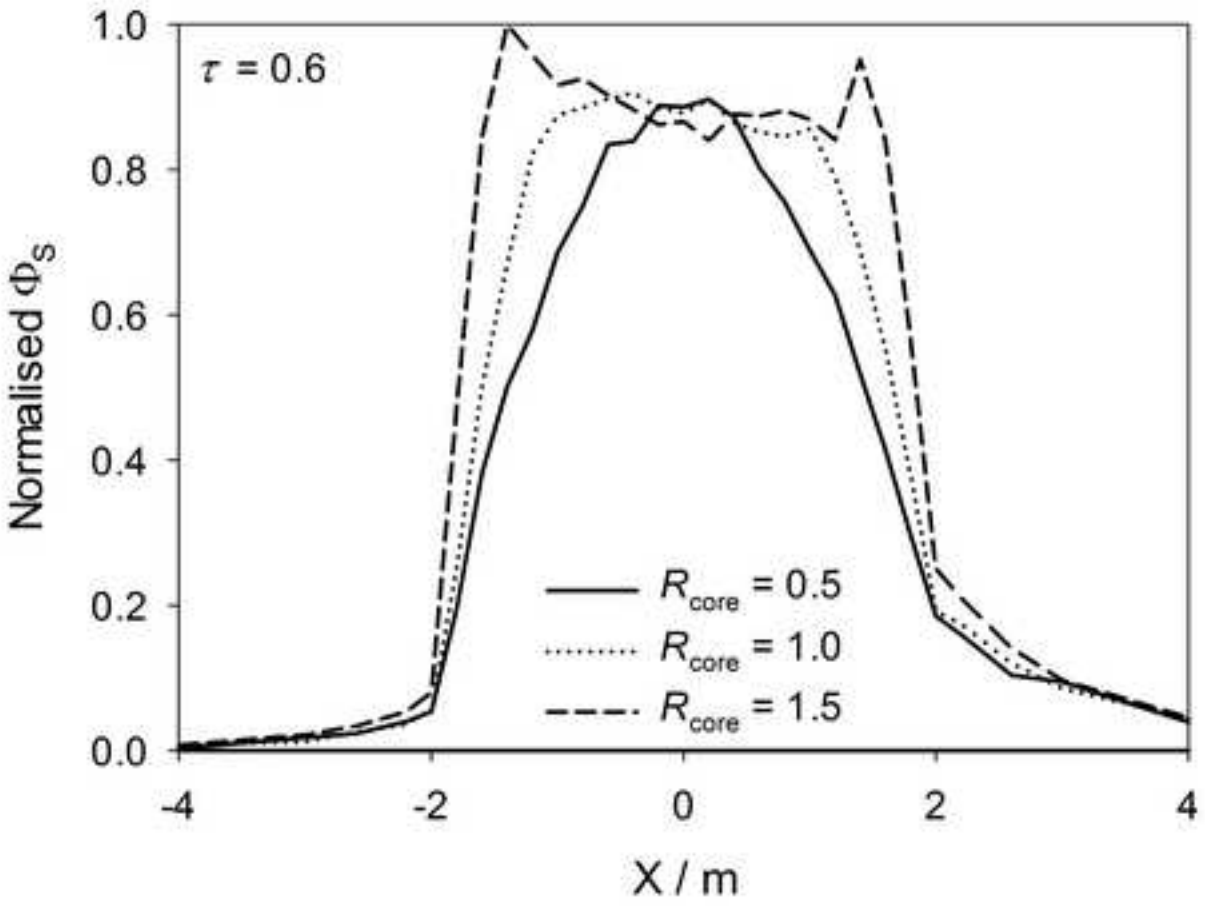

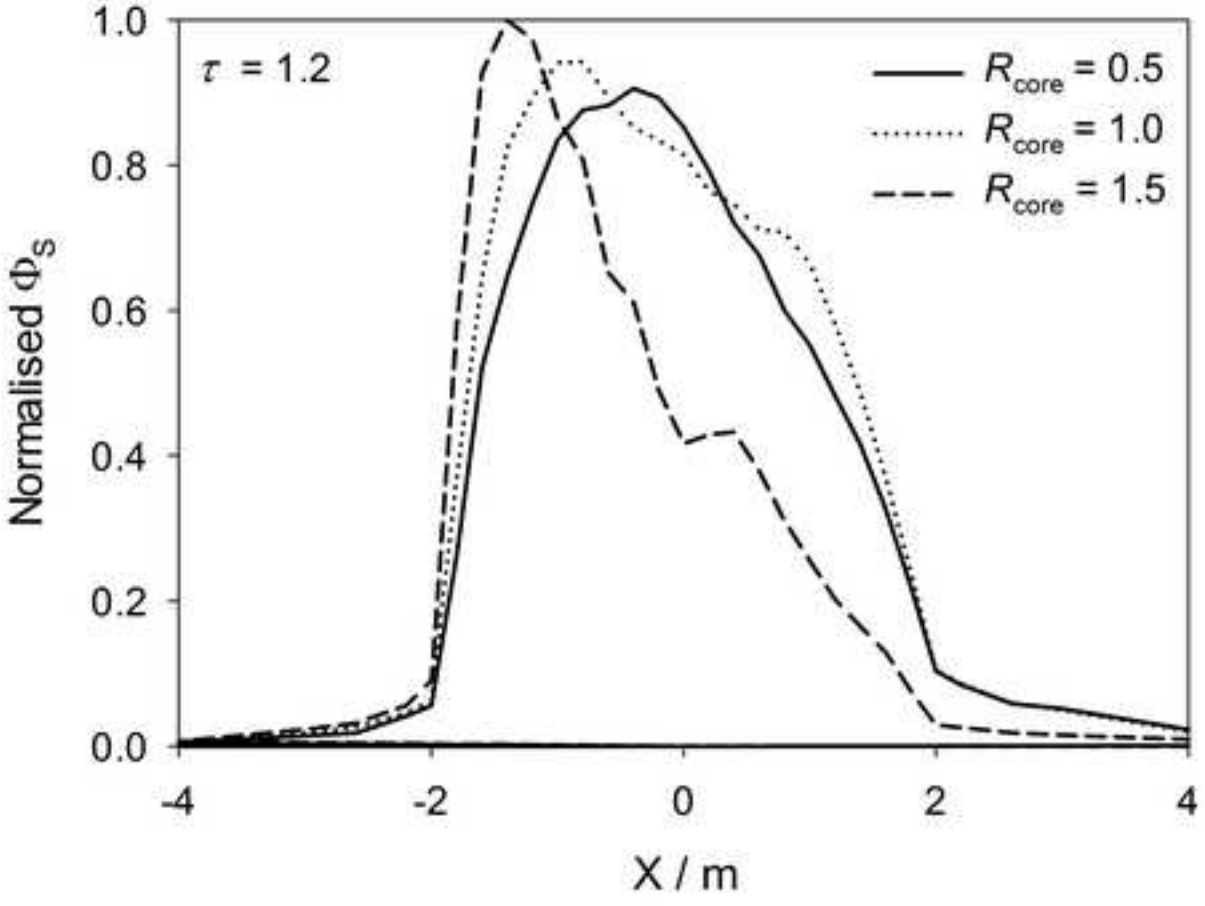

Figure 10

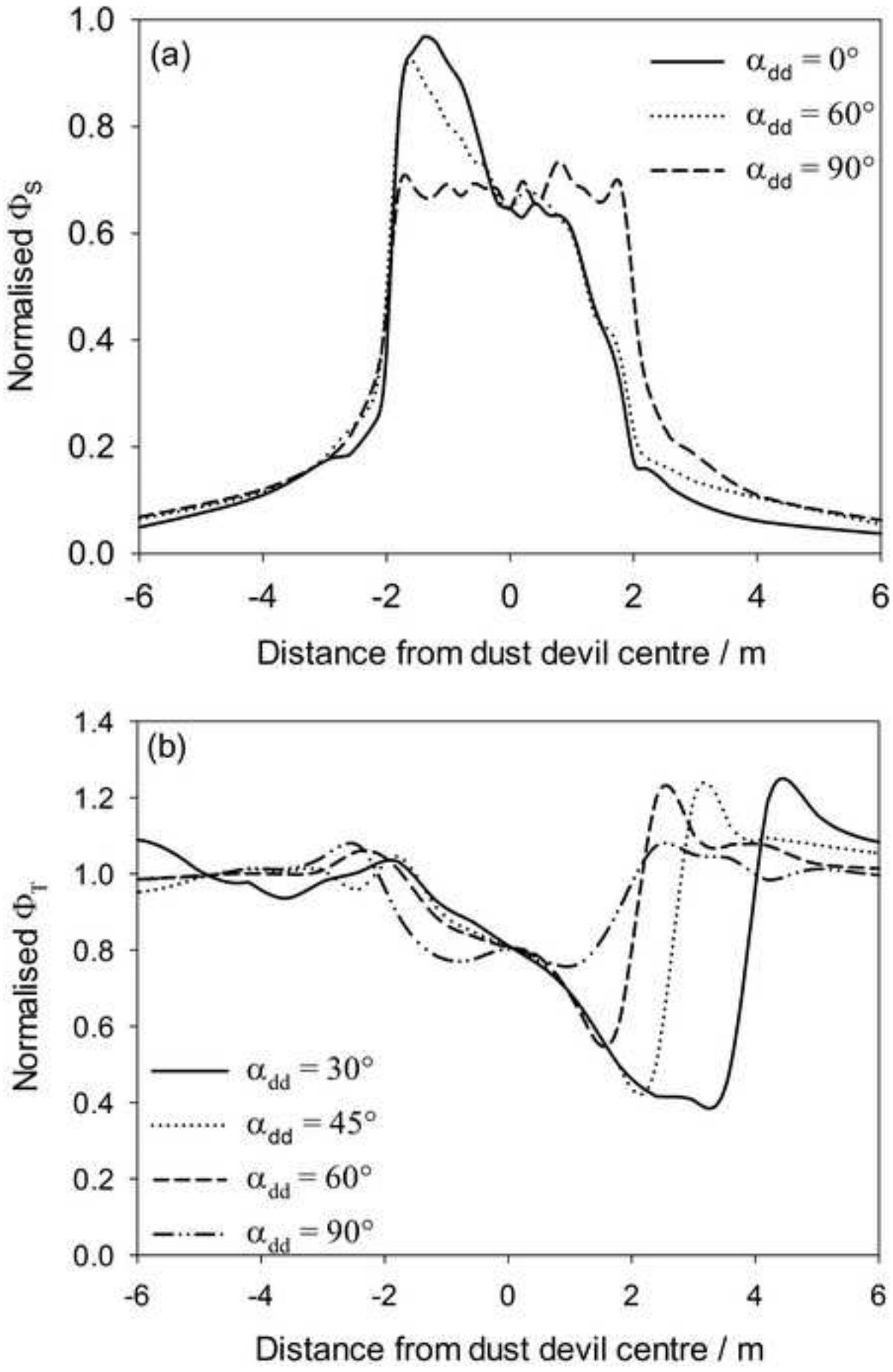

Figure 11

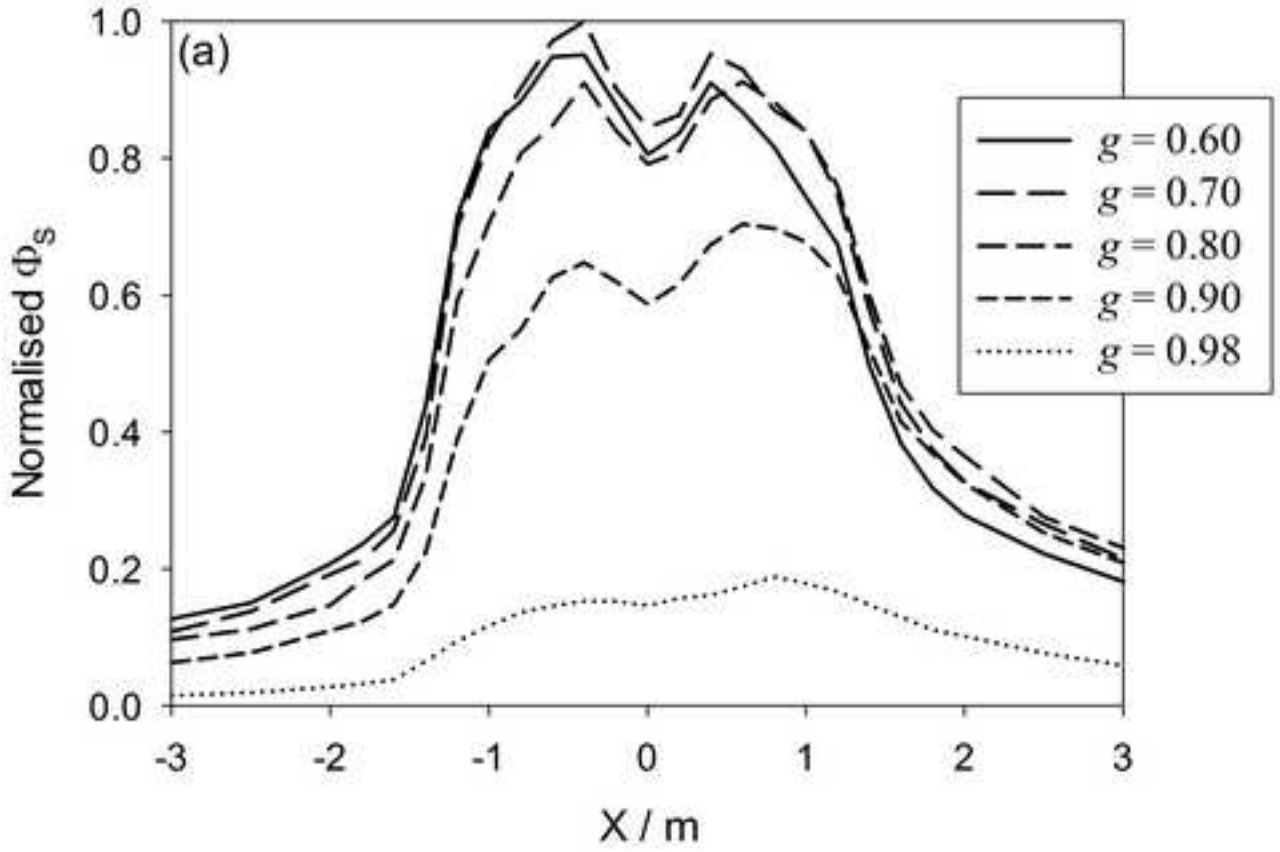

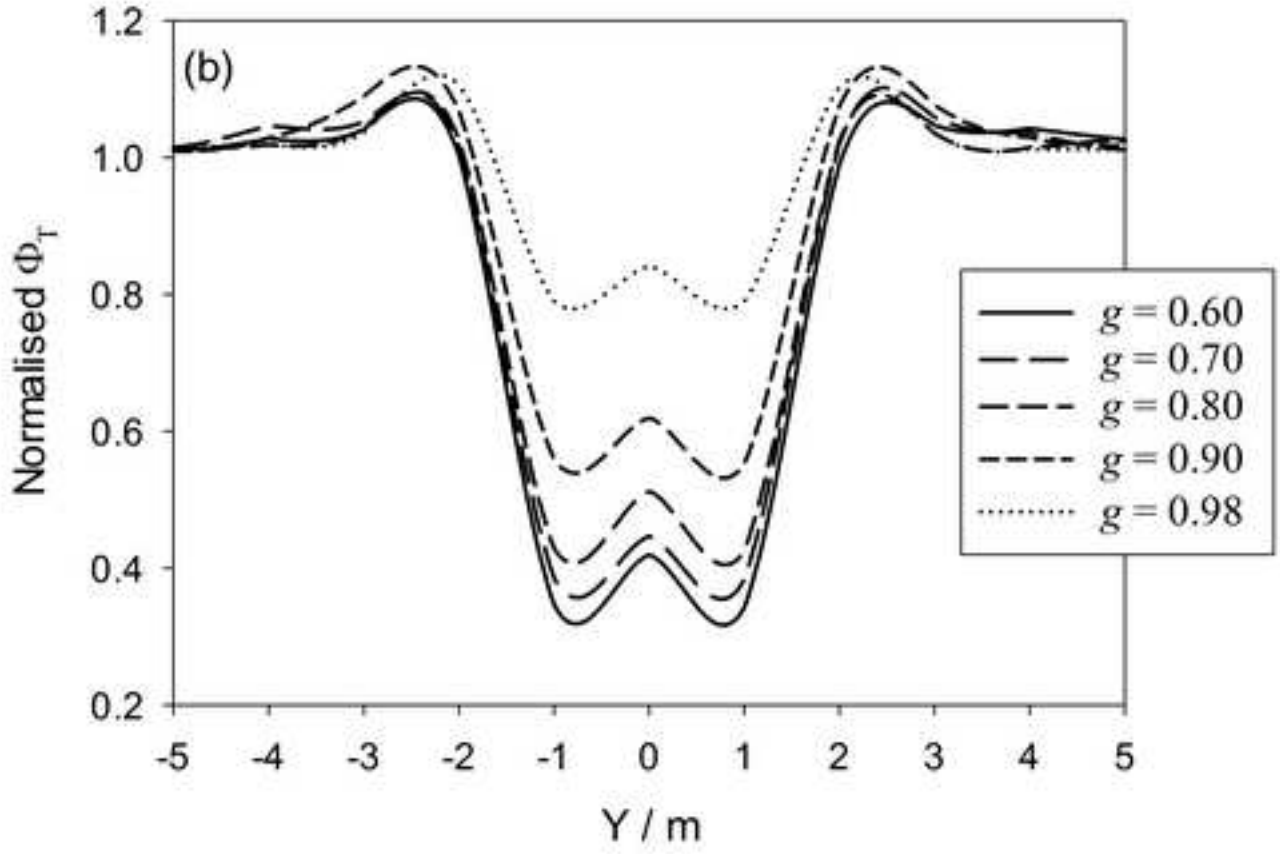

Figure 12

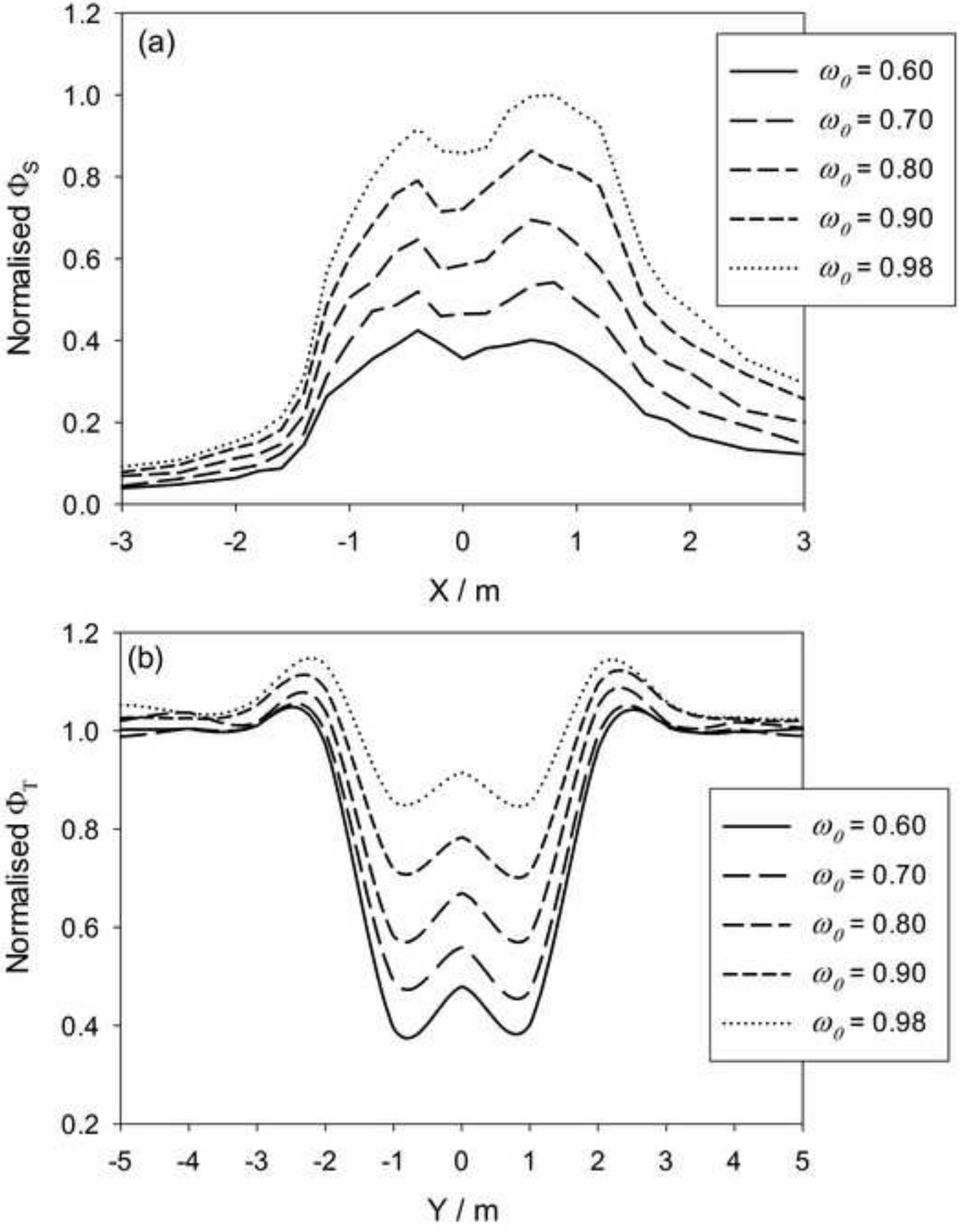

Dust optical depth	k_{ext} / m^{-1}					
	Scenario 1		**Scenario 2**		**Scenario 3**	
	Core	Wall	Core	Wall	Core	Wall
0.15	0.019	0.056	0.025	0.050	0.030	0.045
0.3	0.038	0.113	0.050	0.100	0.060	0.090
0.6	0.075	0.225	0.100	0.200	0.120	0.180
0.9	0.113	0.338	0.150	0.300	0.180	0.270
1.2	0.150	0.450	0.200	0.400	0.240	0.360
1.6	0.200	0.600	0.267	0.533	0.320	0.480
2.0	0.250	0.750	0.333	0.667	0.400	0.600

We study light transmission through dust devils with a Monte Carlo scattering model
The scattered flux is highly dependent on the internal dust distribution
The direct flux is dependent on the total amount of dust present
A solar zenith angle bias acts on the asymmetry parameter in the scattered flux
Measurement of total *and* scattered flux is crucial for characterising dust devils